Journal of Power Sources 248 (2014) 388–395

Contents lists available at ScienceDirect

Journal of Power Sources

journal homepage: www.elsevier.com/locate/jpowsour

$NaAlH_4$ dehydrogenation properties enhanced by $MnFe_2O_4$ nanoparticles

Qi Wan [a], Ping Li [a,*], Ziliang Li [a], Kuifei Zhao [a], Zhiwei Liu [a], Ling Wang [a], Fuqiang Zhai [b], Xuanhui Qu [a,c], Alex A. Volinsky [d]

[a] Institute for Advanced Materials and Technology, University of Science and Technology Beijing, Beijing 100083, China
[b] Departament Física Aplicada, EETAC, Universitat Politècnica de Catalunya – BarcelonaTech, 08860 Castelldefels, Spain
[c] State Key Laboratory for Advanced Metals and Materials, University of Science and Technology Beijing, Beijing 100083, China
[d] Department of Mechanical Engineering, University of South Florida, Tampa, FL 33620, USA

HIGHLIGHTS

- Nanosized $MnFe_2O_4$ effect on $NaAlH_4$ desorption properties is studied for the first time.
- $NaAlH_4$ + 7 mol% $MnFe_2O_4$ desorption temperature onset is much lower than pristine $NaAlH_4$.
- The apparent activation energy of the $MnFe_2O_4$ doped sample is dramatically decreased.
- Mn species and $Fe_{0.9536}O$ phases significantly improve $NaAlH_4$ desorption properties.

ARTICLE INFO

Article history:
Received 17 June 2013
Received in revised form
5 September 2013
Accepted 22 September 2013
Available online 2 October 2013

Keywords:
Manganese ferrite
Hydrogen storage
Sodium alanate
Dehydriding temperature
Apparent activation energy

ABSTRACT

The catalytic effects of $MnFe_2O_4$ nanoparticles on the dehydrogenation properties of $NaAlH_4$, prepared by ball milling, are investigated. The onset temperatures for $NaAlH_4$ + 7 mol% $MnFe_2O_4$ are 95 °C, 152 °C and 327 °C for the three dehydrogenation steps, significantly lower compared with as-received $NaAlH_4$. The isothermal dehydriding kinetics shows that adding $MnFe_2O_4$ to $NaAlH_4$ could significantly enhance the desorption kinetics of $NaAlH_4$, 7 mol% $MnFe_2O_4$-doped sample also displays the well-maintained kinetics and only a slight capacity loss for the three cycles. From the differential scanning calorimetry and the Kissinger desorption kinetics analysis, the apparent activation energy of the 7 mol% $MnFe_2O_4$-doped sample for the three steps is 57.74 kJ mol^{-1}, 75.06 kJ mol^{-1} and 117.22 kJ mol^{-1}, resulting in 56.05 kJ mol^{-1}, 67.53 kJ mol^{-1} and 59.12 kJ mol^{-1} reduction, respectively, compared with the as-received $NaAlH_4$. Based on the Fourier Transform Infrared Spectroscopy, X-ray diffraction and X-ray photoelectron spectroscopy, $Fe_{0.9536}O$ and amorphous Mn or Mn-containing species together play a synergistic role in remarkably improving $NaAlH_4$ dehydriding properties.

1. Introduction

Solid-state lightweight metal complex hydrides have received increased attention due to their high volumetric and gravimetric hydrogen storage density [1–6], which may meet the U.S. Department of Energy 2015 targets [7]. A viable hydrogen storage system requires hydrogen storage materials with more than 5.5 wt% capacity and fast desorption kinetics. Among various complex metal hydrides [1,8–17], sodium alanates are considered to be a promising solid-state hydrogen storage media, since Bogdanović and Schwickardi [18] reported that $NaAlH_4$ could reversibly desorb hydrogen under moderate conditions after doping with Ti-containing catalyst. The absorption capacity decreases with the increasing of cycles, which declines from 4.2 wt% to 3.1 wt% at 170 °C under 15 MPa hydrogen pressure and from 2.7 wt% to 2.1 wt % at 200 °C under 6 MPa hydrogen pressure over 35 cycles, respectively. Upon heating, $NaAlH_4$ would decompose to release hydrogen in three steps according to the following reactions:

$$3NaAlH_4 \rightarrow Na_3AlH_6 + 2Al + 3H_2 \quad (3.7\ wt\%) \tag{1}$$

$$Na_3AlH_6 \rightarrow 3NaH + Al + 1.5H_2 \quad (1.9\ wt\%) \tag{2}$$

$$3NaH \rightarrow 3Na + 1.5H_2 \quad (1.8\ wt\%) \tag{3}$$

Reaction (1) happens at the temperature range of 170–230 °C, reactions (2) and (3) initiate above 250 °C and 400 °C, respectively.

* Corresponding author.
E-mail address: ustbliping@126.com (P. Li).

0378-7753/$ – see front matter © 2013 Elsevier B.V. All rights reserved.
http://dx.doi.org/10.1016/j.jpowsour.2013.09.093

However, high desorption temperature, sluggish dehydrogenation kinetics and poor reversibility limit $NaAlH_4$ practical applications [6,19–21]. During the past decade researchers have been trying to overcome these drawbacks. The efforts included preparing nanocrystalline $NaAlH_4$ [6,22–24], and adding metal catalysts [25–29], C species [20,30,31], metal halides [21,32–37], metal oxides [2,5,19,38–40] and other compounds [3,41–43]. For improvement of dehydriding properties of $NaAlH_4$, generally, metal halides have better catalytic effect than metal oxides, metal oxides have better catalytic effect than metals, but some metal oxide has better catalytic effect than metal halide, such as $Nb_2O_5 > NbF_5$. Usually, the dehydriding temperature and dehydriding kinetics can be strikingly improved by adding catalyst, but the dehydriding capacity decreases remarkably with the increase of cycles [2,27,47]. Naik et al. demonstrated the superior effects of Mn^{2+} on improving the dehydrogenation properties of $NaAlH_4$ [35]. It was also reported that Fe and Fe^{3+} could ameliorate $NaAlH_4$ hydrogen storage performance [29,44]. Moreover, Zhai et al. [45] reported that $MnFe_2O_4$ could remarkably improve $LiAlH_4$ dehydrogenation. $MnFe_2O_4$ has better catalytic effect than Fe or Mn oxides alone in improving the dehydriding properties of $LiAlH_4$, $NaAlH_4$ has similar performances with $LiAlH_4$. Therefore, it is reasonable to assume that $MnFe_2O_4$ would show great potential as a catalyst to advance $NaAlH_4$ hydrogen storage performance. Motivated by the above findings, in the present work, $MnFe_2O_4$ nanoparticles were employed as catalyst precursors to study their effect on the dehydrogenation properties of $NaAlH_4$ prepared by ball milling.

2. Experimental

$NaAlH_4$ (≥93% purity) was purchased from Sigma Aldrich Co., and $MnFe_2O_4$ (≥99.99% purity, 20 nm particle size) was prepared by the nitrate–citrate auto-combustion methods. The details of the preparation procedure are given in the previous report [46]. Both materials were used directly, without any further purification. All handling (including weighing and loading) was performed in a high-purity argon-filled glove box in order to avoid oxidation and moisture. About 3 g of $NaAlH_4$ was mixed with different mole fractions (3 mol%, 5 mol%, 7 mol%, and 9 mol%) of $MnFe_2O_4$ nanoparticles, and then ball milled for 30 min in a high-energy Spex Mill. All the samples were loaded into the stainless steel vial in an argon-filled glove box. ZrO_2 balls were added with a ball-to-powder weight ratio of 15:1. The samples were ball milled for 10 min and then cooled down for 5 min after each cycle.

The dehydrogenation properties of as-received $NaAlH_4$ and doped samples were measured using a pressure–composition–temperature (PCT) apparatus (Beijing Nonferrous Metal Research Institute, China). For non-isothermal dehydrogenation, 0.5 g of the sample was loaded into the vessel, and then heated up to 500 °C at a 4 °C min^{-1} rate under 0.01 MPa atm pressure. The isothermal dehydrogenation measurements for the undoped and doped samples were performed at 120 °C and 150 °C under a hard vacuum atmosphere. Following the first complete dehydrogenation, the samples were subjected to rehydrogenation studies at 150 °C under 5 MPa hydrogen pressure for 180 min. Subsequently, the rehydrogenated samples were dehydrogenated at similar temperature.

In order to further analyze the dehydrogenation performance and calculate the desorption activation energy of the doped $NaAlH_4$ sample by means of the Kissinger method, the differential scanning calorimetry (DSC) was performed using NETZSCH STA 449C in high-purity argon (50 mL min^{-1} flow rate, 99.999% pure). About 5 mg of the sample was sealed into a 50 mL alumina crucible in the glove box, and then heated at different rates (4 °C min^{-1}, 7 °C min^{-1} and 10 °C min^{-1}), from 50 °C to 500 °C.

The morphology of the as-received and doped samples after ball milling was examined by scanning electron microscopy (SEM, ZEISS EVO18, Germany). The phase structure of the samples after ball milling and after dehydrogenation was determined by using the MXP21VAHF X-ray diffractometer (XRD with Cu Kα radiation, 40 kV, 200 mA) at room temperature. The 2θ angle was varied from 25° to 90° in 0.02° increments, 1 s per step. The samples were covered with the paraffin film to prevent oxidation during the XRD test.

Fourier transformation infrared spectroscopy was performed by using an infrared spectrophotometer (NEXUS670). The spectral resolution was 4 cm^{-1}. Scans were performed between 500 cm^{-1} and 2000 cm^{-1} in argon. X-ray photoelectron spectroscopy (XPS) experiments were performed in an ultra high vacuum (UHV) chamber with the base pressure of around 3×10^{-13} Pa, equipped with a Perkin–Elmer PHI-5300 XPS spectrometer.

3. Results and discussion

3.1. Dehydrogenation temperature

Fig. 1 shows the non-isothermal desorption curves of as-received $NaAlH_4$, as-milled $NaAlH_4$ and ball-milled $NaAlH_4$ doped with 3 mol%, 5 mol%, 7 mol% and 9 mol% $MnFe_2O_4$ nanopowders. The desorption curves clearly reveal that adding $MnFe_2O_4$ nanoparticles dramatically improves $NaAlH_4$ dehydriding properties, resulting in a striking reduction of the onset desorption temperature, not only for the first and second steps, but also for the third step. The onset desorption temperature for all doped samples is below 130 °C, indicating a significant decrease compared with the as-received $NaAlH_4$. For the as-received $NaAlH_4$, it starts to decompose at 179 °C, and weight loss is about 5.18 wt% after heating to 290 °C. The third step commences at 411 °C, and a hydrogen release capacity of 6.4 wt% is obtained below 450 °C. Compared with as-received $NaAlH_4$, the onset desorption temperature of as-milled $NaAlH_4$ decreased slightly by 14 °C, 11 °C and 13 °C for the three steps, respectively, due to the $NaAlH_4$ activation introduced by the ball milling [2,36].

When doping $MnFe_2O_4$ nanoparticles to the $NaAlH_4$ matrix, the onset desorption temperature of $NaAlH_4$ is further reduced. For the 3 mol% doped sample, the dehydrogenation process starts at 125 °C for the first stage, and initiates at 180 °C and 367 °C for the second

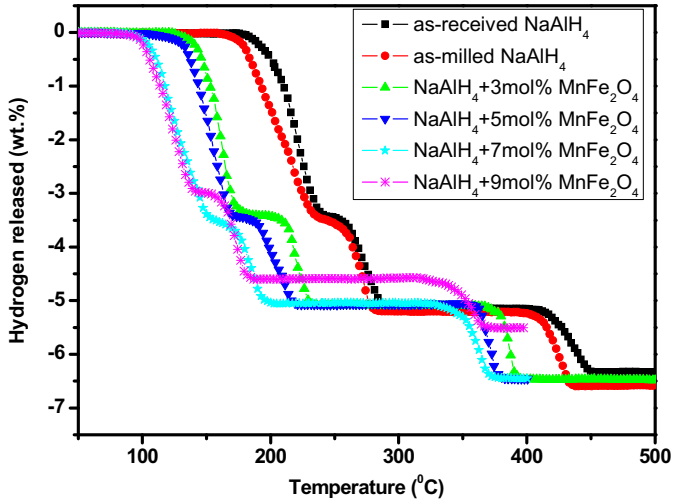

Fig. 1. Thermal desorption curves of the as-received $NaAlH_4$, as-milled $NaAlH_4$, and ball-milled $NaAlH_4$ doped with 3 mol%, 5 mol%, 7 mol% and 9 mol% nanosized $MnFe_2O_4$.

and the third steps, respectively. Further increase of the additives amount to 5 mol% reduces the onset dehydrogenation temperature to 115 °C for the first stage. Compared with as-received $NaAlH_4$, adding 3 mol% and 5 mol% of $MnFe_2O_4$ causes a reduction in the onset desorption temperature of 54 °C and 64 °C for the first step, 60 °C and 75 °C for the second step, and 44 °C and 56 °C for the third step, respectively. During the three dehydrogenation processes, the sample with 3 mol% $MnFe_2O_4$ releases about 3.42 wt% hydrogen for the first stage, 5.12 wt% hydrogen for the first two stages, 6.79 wt% hydrogen for three stages, whereas 3.41 wt%, 5.10 wt%, and 6.75 wt% hydrogen is desorbed for these of the 5 mol% doped sample, respectively. 7 mol% $MnFe_2O_4$ has the onset temperatures for the three steps of 95 °C, 152 °C and 327 °C, respectively, resulting in further decrease, compared with the 3 mol% and 5 mol% doped samples, and a reduction of 84 °C, 88 °C and 84 °C, respectively, compared with the as-received $NaAlH_4$. Meanwhile, the 7 mol% doped sample releases 3.40 wt%, 5.08 wt%, and 6.71 wt% hydrogen in the first step, the first two steps, and three dehydrogenation steps, respectively. With the $MnFe_2O_4$ amount increasing to 9 mol%, the onset dehydrogenation temperature reduces to 90 °C, 140 °C and 319 °C, respectively, which demonstrates $MnFe_2O_4$ superiority in improving the $NaAlH_4$ desorption temperature, compared with other various catalysts reported in the literature [2,5,31,33,35,36,40,47]. However, the desorption hydrogen content for the 9 mol% doped sample is only 2.89 wt%, 4.59 wt%, and 5.51 wt% for the first step, the first two steps, and the three steps, respectively, signifying a drastic reduction in the released hydrogen capacity due to an excess amount of $MnFe_2O_4$ nanoparticles. The decrease in hydrogen storage capacity may be associated with the impurity in the original $NaAlH_4$ powder, the amount of catalyst, and some partial decomposition of $NaAlH_4$ during high-energy ball milling with $MnFe_2O_4$ nanoparticles, despite the air-cooling of the vial employs during the milling process, the localized impact associated with the ball milling induces the localized temperature increase of the $NaAlH_4$ powders being ball-milled and heavily catalyzed with $MnFe_2O_4$ nanoparticles. We assume that the simultaneous effect of both the temperature increase during milling and catalyst causes the partial decomposition of $NaAlH_4$. For the small additions, the loss in capacity is insignificant owing to the moderate exposure of $NaAlH_4$ to catalyst, as reported in the literature [36,45,48]. Therefore, the $NaAlH_4$ + 7 mol% $MnFe_2O_4$ sample exhibits optimal dehydrogenation performance, including the onset dehydrogenation temperature and the released hydrogen capacity. Thus, using the optimal 7 mol% amount of $MnFe_2O_4$ nanoparticles, allows analyzing the $MnFe_2O_4$ mechanism and the catalytic effect in the following tests.

To further compare the thermal decomposition behavior of $NaAlH_4$, with and without $MnFe_2O_4$ doping, Fig. 2 shows DSC curves of the as-received $NaAlH_4$ and $NaAlH_4$ doped with 7 mol% $MnFe_2O_4$ samples within the 50–500 °C temperature range (4 °C min^{-1} heating rate). As presented in Fig. 2(a), the DSC curve of the as-received $NaAlH_4$ includes six distinct peaks, corresponding to one exothermic process and five endothermic processes. The first exothermic process appears at 173.1 °C, corresponding to the interaction of $NaAlH_4$ with surface hydroxyl impurities, as reported in other papers [2,48,49]. The first endothermic peak at 182.5 °C arises from $NaAlH_4$ melting [36,43]. The second endothermic peak occurs at 239.6 °C due to dehydrogenation of $NaAlH_4$ to Na_3AlH_6. The third endothermic peak at 252.6 °C can be attributed to a phase transition of α-Na_3AlH_6 to β-Na_3AlH_6 [2,36]. The fourth and fifth endothermic peaks at 270.4 °C and 433.5 °C are assigned to the dehydrogenation of Na_3AlH_6 and NaH, respectively. In contrast, the features of the $MnFe_2O_4$-doped sample composite are strikingly different, displaying only three characteristic endothermic peaks in the DSC plot seen in Fig. 2(b). These three endothermic peaks at

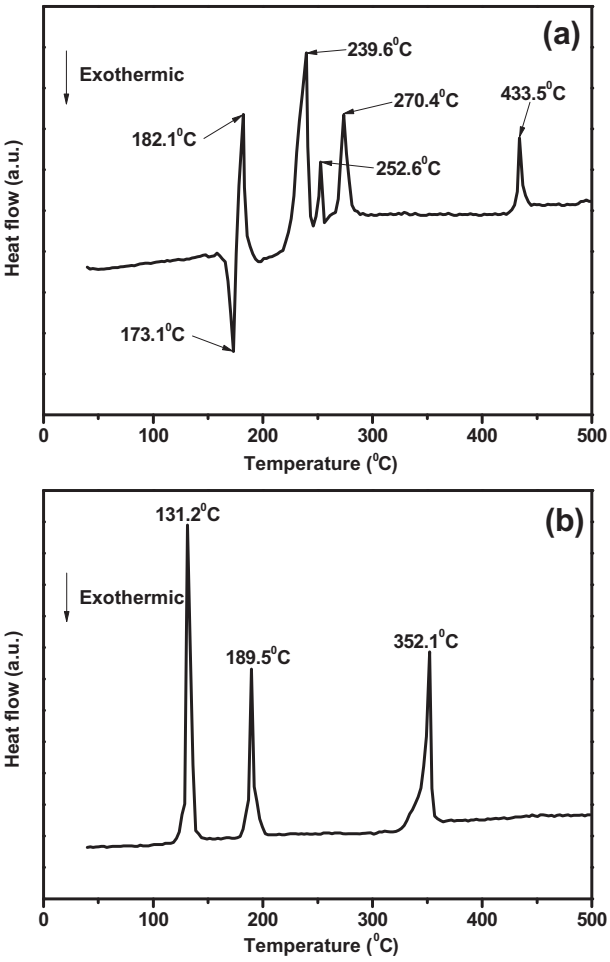

Fig. 2. DSC profiles of (a) as-received $NaAlH_4$ and (b) ball-milled $NaAlH_4$ doped with 7 mol% $MnFe_2O_4$ within the 50–500 °C temperature range (4 °C min^{-1} heating rate).

131.2 °C, 189.5 °C and 352.1 °C correspond to the dehydrogenation of $NaAlH_4$, Na_3AlH_6 and NaH, respectively, which is similar with the DSC results of $NaAlH_4$ doped with various catalysts reported in the literature [3,35,36,47,50–55].

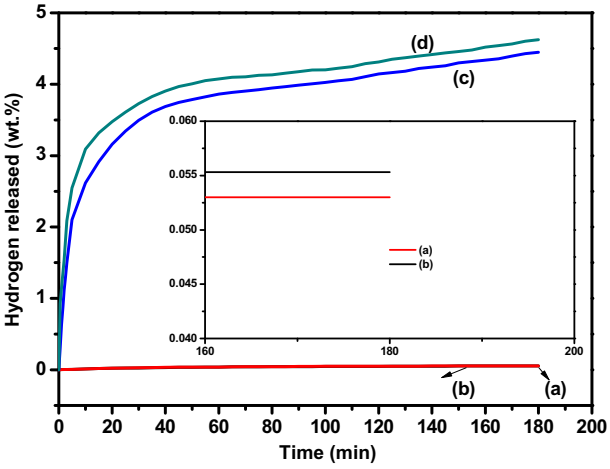

Fig. 3. Isothermal desorption curves of (a) as-received $NaAlH_4$ at 150 °C, (b) as-milled $NaAlH_4$ at 150 °C, and ball-milled $NaAlH_4$ doped with 7 mol% $MnFe_2O_4$ at (c) 120 °C and at (d) 150 °C.

The notable reduction of the peak temperature in the above DSC results shows that the dehydrogenation properties of $NaAlH_4$ are significantly improved by adding nanosized $MnFe_2O_4$. Nevertheless, it is noteworthy that the desorption temperature onset measured by DSC is quite higher than that measured by PCT. A similar phenomenon is also reported in the literature [2,3,36]. This is mainly due to the different dehydrogenation atmospheres for the samples tested with DSC (0.1 MPa argon) and PCT (0.01 MPa atm), resulting in different driving forces during the dehydriding process.

3.2. Dehydrogenation kinetics

The excellent effect of $MnFe_2O_4$ nanopowders on promoting the dehydriding kinetics of $NaAlH_4$, in comparison with the as-received $NaAlH_4$ and as-milled $NaAlH_4$ samples, is further demonstrated by examination of isothermal hydrogen desorption at different temperatures (Fig. 3). Fig. 3 shows isothermal desorption kinetics curves of as-received $NaAlH_4$ and as-milled $NaAlH_4$ at 150 °C and $NaAlH_4$ + 7 mol% $MnFe_2O_4$ samples at 120 °C and 150 °C, respectively. For the as-received $NaAlH_4$ and as-milled $NaAlH_4$, only 0.05 wt% hydrogen is released at 150 °C after 180 min for both samples, indicating poor dehydriding kinetics of as-received $NaAlH_4$ and as-milled $NaAlH_4$. However, $NaAlH_4$ + 7 mol% $MnFe_2O_4$ releases 4.43 wt% hydrogen at 120 °C in 180 min. Further temperature increase to 150 °C results in 4.67 wt% of released hydrogen for the same time. Moreover, the doped sample desorbs about 3.11 wt% hydrogen in 10 min at 150 °C, which demonstrates $MnFe_2O_4$ superiority in improving $NaAlH_4$ desorption kinetics, compared with other catalysts reported in the literature [2,3,5,26,36]. Therefore, dramatic improvement of $NaAlH_4$ dehydrogenation kinetics can be achieved by adding $MnFe_2O_4$ nanopowders.

Further study indicates that the catalytic enhancement arising upon adding $MnFe_2O_4$ persists well in dehydrogenation/rehydrogenation cycles. Fig. 4 brings out the results of the first three rehydrogenations of 7 mol% $MnFe_2O_4$-doped sample at 150 °C under 5 MPa hydrogen pressure for 180 min. 7 mol% $MnFe_2O_4$-doped sample exhibits a slow decrease in hydrogen absorption capacity, from about 3.90 wt% to about 3.81 wt% in the three cycles. The dehydriding curves of ball-milled $NaAlH_4$ doped with 7 mol% $MnFe_2O_4$ at 150 °C after the rehydrogenation are shown in Fig. 5. 7 mol% $MnFe_2O_4$-doped sample also displays the well-maintained kinetics and only a slight capacity loss for the three cycles, it declines from 3.76 wt% to 3.64 wt% in 180 min. Thus, dramatic improvement of $NaAlH_4$ rehydrogenation/dehydrogenation properties can be achieved by adding $MnFe_2O_4$ nanopowders.

3.3. Dehydrogenation mechanism

SEM images of the as-received $NaAlH_4$ and the ball-milled $NaAlH_4$ sample doped with 7 mol% $MnFe_2O_4$ nanopowders are presented in Fig. 6. The particle size of the as-received $NaAlH_4$ is larger than 100 μm, however, the particle size of the $MnFe_2O_4$-doped sample is between 3 μm and 8 μm. It must be mentioned that the embedded $MnFe_2O_4$ particles cannot be seen on the $NaAlH_4$ surface by SEM because of their extremely small size. The dehydriding properties of $NaAlH_4$ doped with $MnFe_2O_4$ are significantly improved after ball milling due to the decreased particle size, which results in high surface defect density and more grain boundaries. Moreover, a high density of nanosized catalyst particles forms a large number of nucleation sites at the surface of the $NaAlH_4$ matrix, leading to surface activation and larger surface area of the $NaAlH_4$ particles.

In order to further analyze $NaAlH_4$ desorption mechanism after doping with $MnFe_2O_4$, the apparent activation energies, E_a, corresponding to $NaAlH_4$, $NaAlH_6$ and NaH decomposition, for both undoped and doped $NaAlH_4$ samples, are obtained from DSC data by using the Kissinger method. Fig. 7 shows the Kissinger plots of as-received $NaAlH_4$ and 7 mol% $MnFe_2O_4$-doped sample. The E_a values of as-received $NaAlH_4$ for the three steps are 113.79 kJ mol^{-1}, 142.59 kJ mol^{-1} and 176.34 kJ mol^{-1}, respectively, while the E_a of the $MnFe_2O_4$-doped sample for the three dehydrogenation steps are calculated to be 57.74 kJ mol^{-1}, 75.06 kJ mol^{-1} and 117.22 kJ mol^{-1}, respectively. Therefore, there is a remarkable reduction of 56.05 kJ mol^{-1}, 67.53 kJ mol^{-1} and 59.12 kJ mol^{-1} in E_a for the three dehydrogenation steps of $NaAlH_4$, indicating that the apparent activation energy is significantly improved by adding $MnFe_2O_4$ nanoparticles. To demonstrate $MnFe_2O_4$ catalytic effect on $NaAlH_4$ dehydrogenation, comparison of E_a for $NaAlH_4$ doped with different catalysts is summarized in Table 1 [2,3,26,33,36,40,43]. $MnFe_2O_4$-doped samples have the lowest apparent activation energy values for the three dehydriding processes, which signifies $MnFe_2O_4$ superiority in improving the desorption performance of $NaAlH_4$, compared with other reported catalysts.

The FTIR spectra of the as-milled $NaAlH_4$, and 3 mol% and 7 mol % $MnFe_2O_4$ doped $NaAlH_4$ samples after ball milling are compared in Fig. 8. It is clear that there is an IR absorption peak at 1440 cm^{-1}

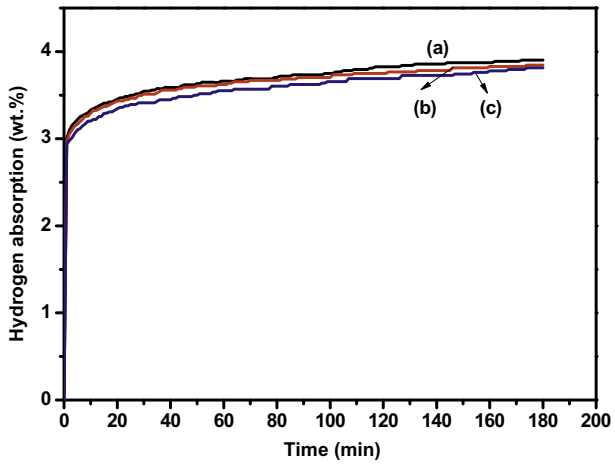

Fig. 4. Rehydrogenation curves of ball-milled $NaAlH_4$ doped with 7 mol% $MnFe_2O_4$ at 150 °C under 5 MPa hydrogen pressure during the first three cycles, (a) the first rehydrogenation, (b) the second rehydrogenation and (c) the third rehydrogenation.

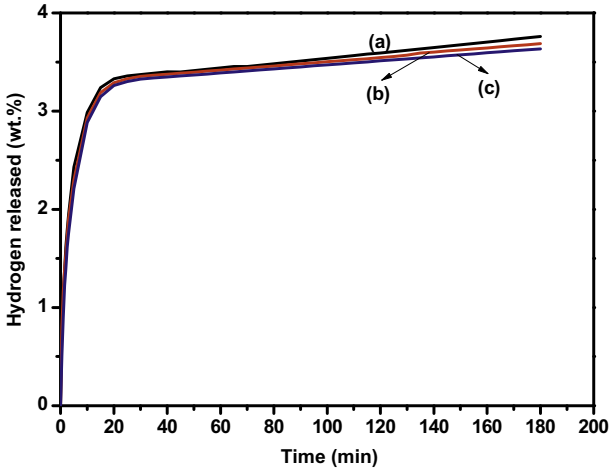

Fig. 5. Dehydriding curves of ball-milled $NaAlH_4$ doped with 7 mol% $MnFe_2O_4$ at 150 °C after the rehydrogenation, (a) after the first rehydrogenation, (b) after the second rehydrogenation, and (c) after the third rehydrogenation.

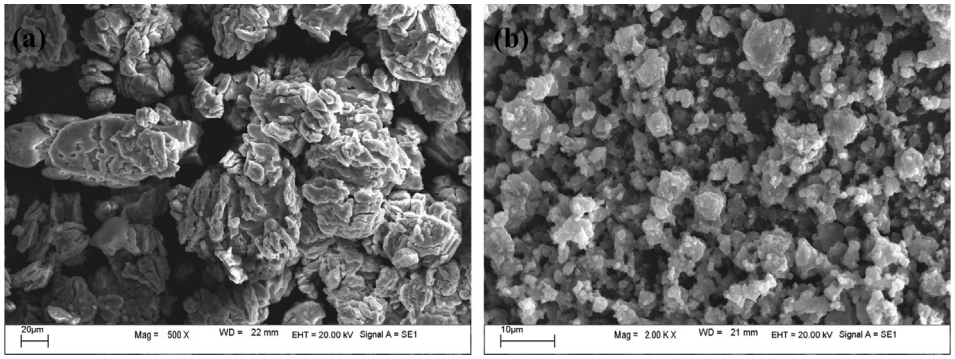

Fig. 6. SEM images of (a) as-received $NaAlH_4$ and (b) ball-milled $NaAlH_4$ doped with 7 mol% $MnFe_2O_4$.

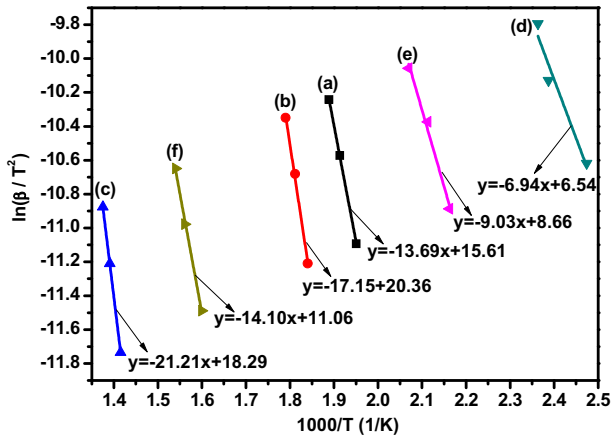

Fig. 7. Kissinger plots for the as-received $NaAlH_4$ (a) the first step, (b) the second step, and (c) the third step and ball-milled $NaAlH_4$ doped with 7 mol% $MnFe_2O_4$, (d) the first step, (e) the second step, and (f) the third step.

for the doped samples. Moreover, the intensity of the IR absorption peak at 1440 cm^{-1} gradually becomes stronger with the increase of $MnFe_2O_4$ amount, which could be ascribed to the appearance of Al–H stretching mode of Na_3AlH_6 [2,41,56]. However, no IR absorption peak exists at the same position in the FTIR spectra of the as-milled $NaAlH_4$ in Fig. 8. For the as-milled $NaAlH_4$, there are two regions of active infrared vibrations of the Al–H bonds: Al–H stretching mode between 1600 and 1700 cm^{-1} and H–Al–H bending modes between 600 and 900 cm^{-1} [26,35,36,41,57]. Na_3AlH_6 also exhibits two regions of active infrared vibrations: Al–H stretching modes between 1200 and 1500 cm^{-1} and H–Al–H bending modes between 600 and 1000 cm^{-1} [2,41,56]. Therefore, it is reasonable to conclude that the doped $NaAlH_4$ sample incurs partial decomposition and yields Na_3AlH_6 during the ball milling process, and the decomposition reaction is processed more severely with the increasing $MnFe_2O_4$ content.

To illustrate that $NaAlH_4$ and $MnFe_2O_4$ react during ball milling, Fig. 9 shows XRD patterns of the as-received $NaAlH_4$ (Fig. 9(a)), as-

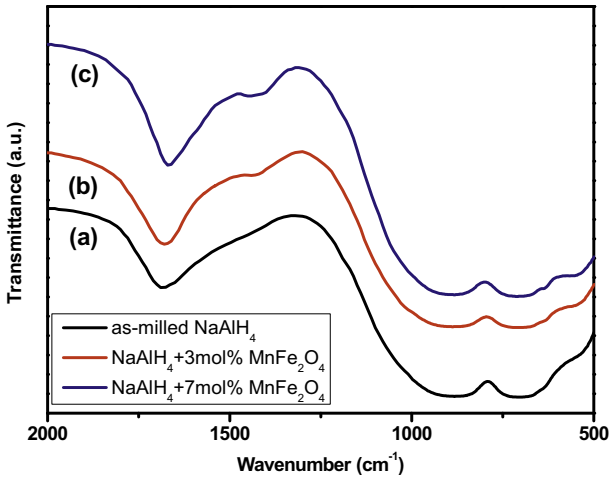

Fig. 8. FTIR spectra of (a) as-milled $NaAlH_4$ and ball-milled $NaAlH_4$ doped with (b) 3 mol% and (c) 7 mol% $MnFe_2O_4$.

Table 1
Activation energy of $NaAlH_4$ doped with different catalysts.

Catalyst	First stage E_a (kJ mol^{-1})		Second stage E_a (kJ mol^{-1})		Third stage E_a (kJ mol^{-1})		Reference
	Before doping	After doping	Before doping	After doping	Before doping	After doping	
TiO_2	116	73	149	101	180	142	[2]
Nb_2O_5	116	65	149	85	180	131	[2]
TiB_2	118.1	106.5	120.7	105.5	–	–	[3]
$CeCl_3$	114.2	80.76	156.8	97.27	–	–	[33]
$CeAl_4$	114.2	80.93	156.8	98.94	–	–	[33]
Co–B	–	67.95	–	–	–	–	[26]
$LaCl_3$	114.2	86.38	162.6	96.11	–	–	[43]
La_3Al_{11}	114.2	92.95	162.6	99.27	–	–	[43]
$SmCl_3$	114.2	88.96	162.6	96.77	–	–	[43]
$SmAl_3$	114.2	91.87	162.6	98.94	–	–	[43]
NbF_5	118.2	88.2	120.9	102.9	–	–	[36]
Ti	119	77	–	–	–	–	[40]
TiO_2	119	67	–	–	–	–	[40]
$MnFe_2O_4$	113.79 ± 0.09	57.74 ± 1.47	142.59 ± 0.88	75.06 ± 0.87	176.34 ± 0.08	117.22 ± 0.68	This work

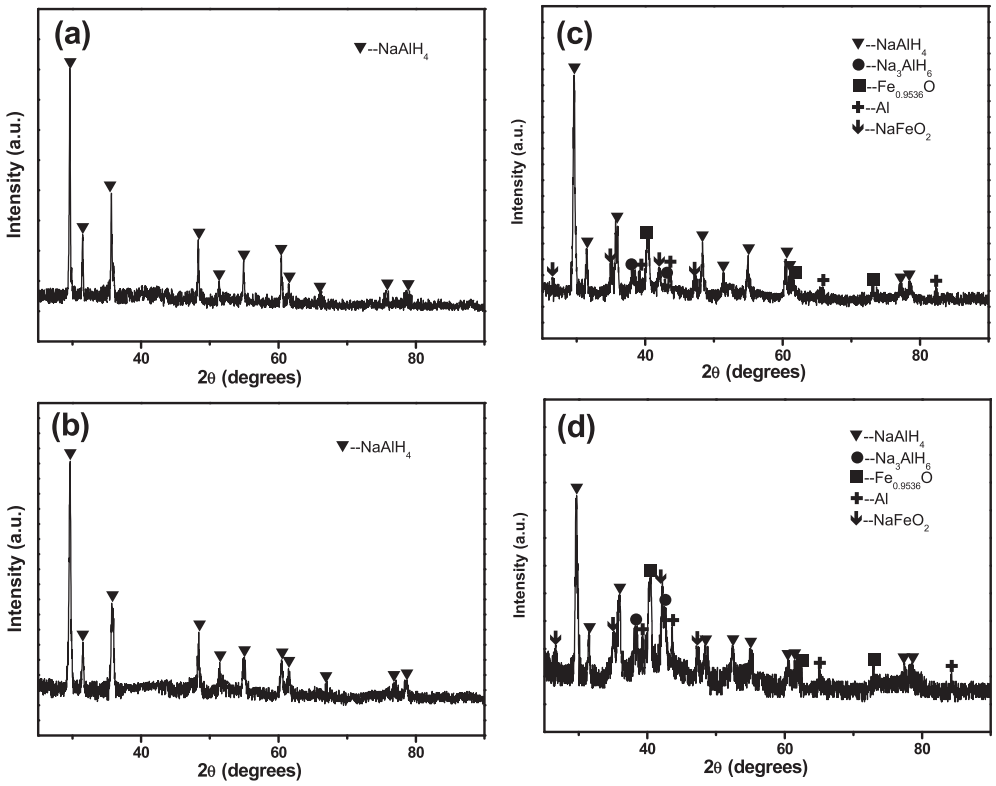

Fig. 9. XRD patterns of (a) as-received $NaAlH_4$, (b) as-milled $NaAlH_4$, and ball-milled $NaAlH_4$ doped with (c) 3 mol% and (d) 7 mol% $MnFe_2O_4$.

milled $NaAlH_4$ (Fig. 9(b)) and $NaAlH_4$ doped with 3 mol% (Fig. 9(c)) and 7 mol% (Fig. 9(d)) $MnFe_2O_4$ after ball milling. For the as-received and as-milled $NaAlH_4$, all diffraction peaks correspond to $NaAlH_4$, and no additional diffraction peaks are detected, indicating that $NaAlH_4$ remains stable during the ball milling process. The stability of $NaAlH_4$ could also be confirmed by the FTIR spectra of as-milled $NaAlH_4$ (Fig. 8). Compared with as-received $NaAlH_4$, diffraction peaks of as-milled $NaAlH_4$ and the doped samples are considerably broadened as a consequence of particle size reduction (also confirmed by SEM), more defects and mechanical strain created within the lattice by ball milling. For the doped samples after ball milling, new phases of Al and Na_3AlH_6 start to appear after adding 3 mol% $MnFe_2O_4$. At the same time, the diffraction peaks of $NaFeO_2$ and $Fe_{0.9536}O$ are observed, for the doped samples in Fig. 9, which indicates that the reaction between $NaAlH_4$ and $MnFe_2O_4$ takes place during ball milling. A similar decomposition reaction occurs between $NaAlH_4$ and Nb_2O_5 [2]. With further increase of the $MnFe_2O_4$ amount, peak intensities of the decomposition products, including Al, Na_3AlH_6, $NaFeO_2$ and $Fe_{0.9536}O$ gradually increase, but $NaAlH_4$ peak intensities decline, suggesting that $NaAlH_4$ reacts with $MnFe_2O_4$ and experiences partial decomposition during ball milling, which becomes more severe with increasing $MnFe_2O_4$ amount. The diffraction peaks of $MnFe_2O_4$ are not detected for all doped samples. It is difficult for the $MnFe_2O_4$ nanoparticles to be distinguished from the noisy background signal, mainly because of their extremely small particle sizes, high dispersion and relatively lower content, resulting in their intrinsically weak X-ray signal, compared with $NaAlH_4$ powders. This phenomenon is in accordance with the reported literature results that TiO_2- [2,39,40] and NbF_5-doped [36] $NaAlH_4$, as also no additives can be detected for those samples after ball milling. It is noteworthy that, although $NaAlH_4$ reacts with $MnFe_2O_4$ and forms $NaFeO_2$ and $Fe_{0.9536}O$ as the decomposition products, there are no diffraction peaks of Mn or Mn-containing species in Fig. 9. It is believed to be mainly due to Mn or Mn-containing phases being in an amorphous state [20,36,49]. It can be concluded that the reaction between $NaAlH_4$ and $MnFe_2O_4$ during ball milling may be as follows:

$$NaAlH_4 + MnFe_2O \rightarrow Na_3AlH_6 + NaFeO_2 + Al + Fe_{0.9536}O + H_2 + MnO_x/Mn \quad (4)$$

In order to determine the phase structures of the doped $NaAlH_4$ samples in the dehydrogenation process, XRD scans are performed on the as-milled $NaAlH_4$ (Fig. 10(a)) as well as 3 mol% (Fig. 10(b)) and 7 mol% (Fig. 10(c)) $MnFe_2O_4$-doped samples after complete desorption, as shown in Fig. 10. For the as-milled $NaAlH_4$, the XRD pattern shows that the sample only has Na and Al phases after desorption. For the doped samples, the XRD patterns imply that there are not only Na and Al phases, but also $NaFeO_2$ and $Fe_{0.9536}O$ phases. The $Fe_{0.9536}O$ reflections intensity gradually increases with the amount of $MnFe_2O_4$. Considering the extreme improvement of $NaAlH_4$ desorption properties by doping $MnFe_2O_4$ nanoparticles, in-situ formed $Fe_{0.9536}O$ acts as a catalyst for $NaAlH_4$ desorption. Meanwhile, although no diffraction peaks of Mn or Mn-containing species could be detected for the doped samples in Fig. 10, it is reasonable to conclude that the Mn or Mn-containing species may also play an important catalytic role for $NaAlH_4$ during the dehydrogenation process.

XPS spectroscopy of $MnFe_2O_4$-doped $NaAlH_4$ is carried out to investigate the nature of the Mn and Fe species after milling. Fig. 11 shows the XPS narrow scan spectra of the ball-milled $NaAlH_4$ doped with 7 mol% $MnFe_2O_4$. Fig. 11(a) shows the photoemission spectrum of Fe 2p at 707.0 eV and 711.8 eV, corresponding to Fe_xO_y and $NaFeO_2$, respectively. Fig. 11(b) shows the photoemission spectrum

of Mn 2p, which is composed of Mn 2p3/2 and Mn 2p1/2 with the binding energy of 640 eV and 652.9 eV, respectively, corresponding to MnO_x/Mn. XPS results further confirm that $NaAlH_4$ and $MnFe_2O_4$ react during ball milling.

Based on the analysis above, it can be concluded that $MnFe_2O_4$ is not the real catalyst, intermediate phases $NaFeO_2$, $Fe_{0.9536}O$ and amorphous MnO_x/Mn formed during ball milling together play a synergistic role in remarkably improving dehydrogenation properties of $NaAlH_4$.

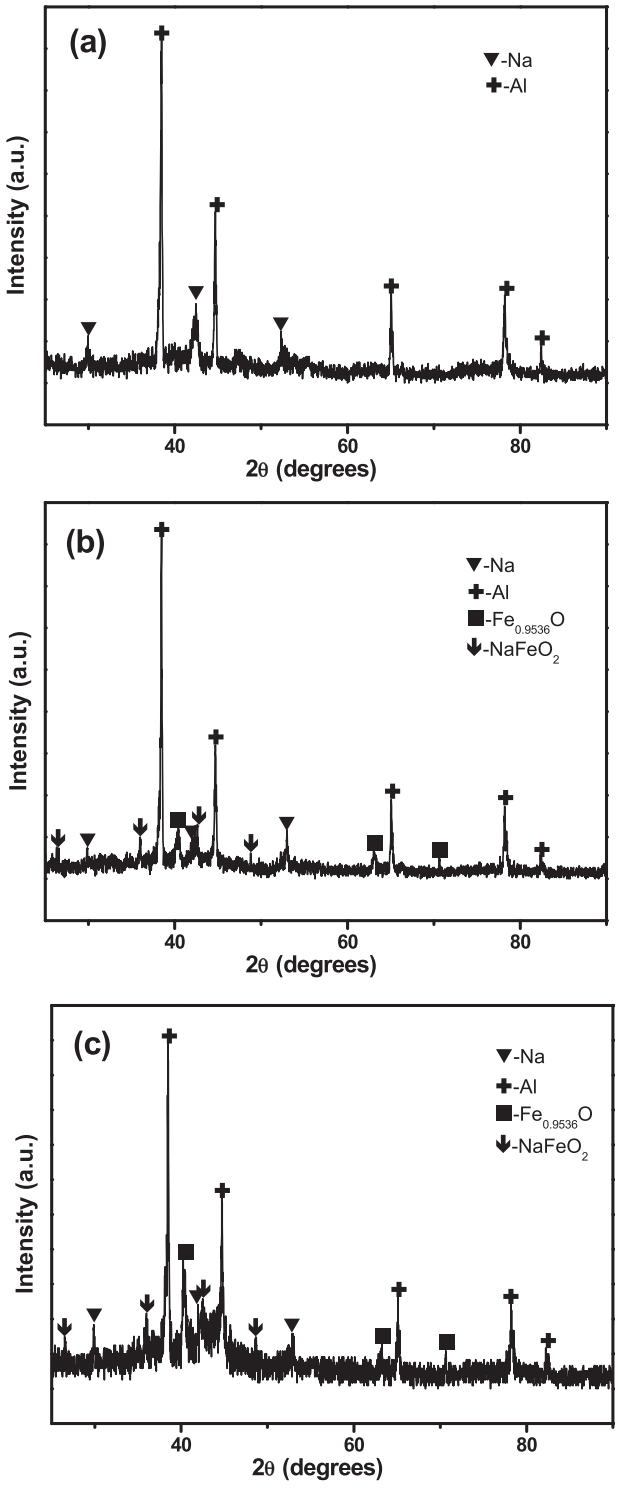

Fig. 10. XRD patterns of (a) as-milled $NaAlH_4$, ball-milled $NaAlH_4$ doped with (b) 3 mol % and (c) 7 mol% $MnFe_2O_4$ after desorption.

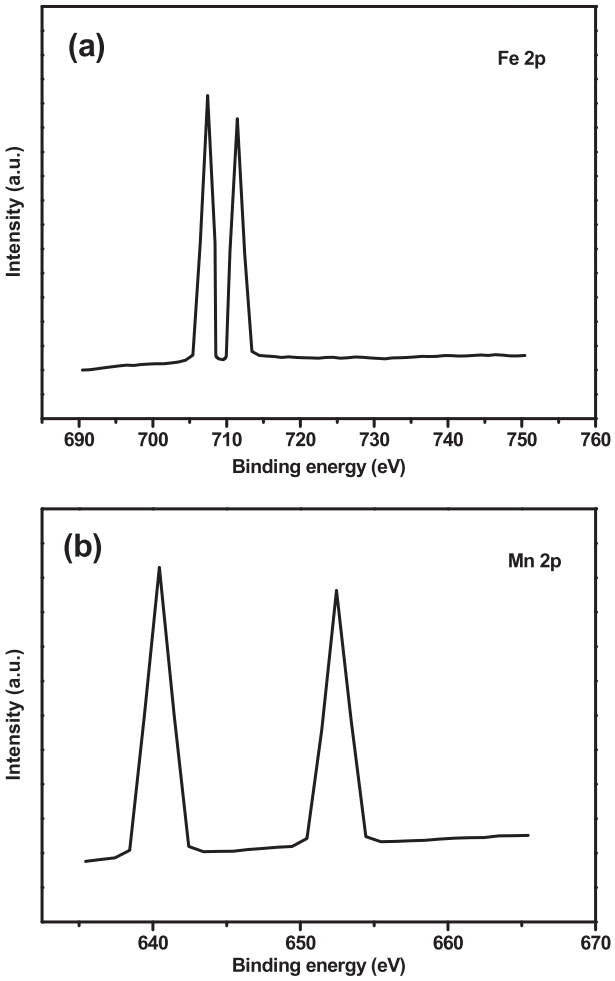

Fig. 11. Narrow scan XPS spectra of $NaAlH_4$ doped with 7 mol% $MnFe_2O_4$ after ball milling (a) Fe 2p and (b) Mn 2p.

4. Conclusions

In conclusion, the dehydrogenation properties of $NaAlH_4$ are remarkably improved by adding $MnFe_2O_4$ nanoparticles. The onset desorption temperature of the ball-milled $NaAlH_4$ doped with 7 mol% $MnFe_2O_4$ is 95 °C, 152 °C and 327 °C for the three steps, releasing 6.71 wt% hydrogen, resulting in 84 °C, 88 °C and 84 °C decrease, respectively, compared with the as-received $NaAlH_4$. The isothermal dehydriding kinetics shows that 7 mol% $MnFe_2O_4$-doped sample can release 4.43 wt% at 120 °C in 180 min. When temperature is increased up to 150 °C, 4.67 wt% is released in 180 min, whereas as-received $NaAlH_4$ only releases 0.05 wt% hydrogen for the same conditions (time and temperature). 7 mol% $MnFe_2O_4$-doped sample also displays the well-maintained kinetics and only a slight capacity loss for the three cycles. This demonstrates that adding $MnFe_2O_4$ to $NaAlH_4$ significantly reduces the decomposition temperature and enhances the desorption kinetics of $NaAlH_4$. From the differential scanning calorimetry and the Kissinger desorption kinetics analysis, the apparent activation energy values of the 7 mol% $MnFe_2O_4$-doped sample for the three steps are 57.74 kJ mol^{-1}, 75.06 kJ mol^{-1} and 117.22 kJ mol^{-1}, resulting in 56.05 kJ mol^{-1}, 67.53 kJ mol^{-1} and 59.12 kJ mol^{-1} reduction, respectively, compared with the as-received $NaAlH_4$

sample. Based on Fourier Transform Infrared Spectroscopy, X-ray diffraction and X-ray photoelectron spectroscopy, $NaFeO_2$, $Fe_{0.9536}O$ and amorphous Mn or Mn-containing species together play a synergistic role in remarkably improving dehydrogenation properties of $NaAlH_4$.

Acknowledgments

The authors acknowledge the financial support from the National High-Tech R&D Program (863 Program) of China (2006AA05Z132).

References

[1] I.P. Jain, P. Jain, A. Jain, J. Alloys Compd. 503 (2010) 303–339.
[2] Rafi-ud-din, X.H. Qu, P. Li, Z. Lin, Q. Wan, M.Z. Iqbal, M.Y. Rafique, J. Phys. Chem. C 116 (2012) 11924–11938.
[3] L. Li, F.Y. Qiu, Y.J. Wang, G. Liu, C. Yan, C.H. An, Y.A. Xu, Y.P. Wang, D.W. Song, L.F. Jiao, H.T. Yuan, Mater. Chem. Phys. 134 (2012) 1197–1202.
[4] S.L. Liu, Q.H. Ma, Z.Z. Liu, X.P. Zheng, Rare Met. Mater. Eng. 40 (2011) 2083–2087.
[5] J. Ma, J. Li, R.Y. Tang, D.W. Li, W.Z. Li, Q.Y. Chen, Int. J. Hydrogen Energy 36 (2011) 9091–9097.
[6] X.L. Fan, X.Z. Xiao, J. Shao, L.T. Zhang, S.Q. Li, H.W. Ge, Q.D. Wang, L.X. Chen, Nano Energy (2013), http://dx.doi.org/10.1016/j.nanoen/2013.03.021.
[7] L.E. Klebanoff, J.O. Keller, Int. J. Hydrogen Energy 38 (2013) 4533–4576.
[8] C. Paduani, P. Jena, Int. J. Hydrogen Energy 38 (2013) 2357–2362.
[9] Y.P. Pang, Y.F. Liu, X. Zhang, M.X. Gao, H.G. Pan, Int. J. Hydrogen Energy 38 (2013) 1460–1468.
[10] J.F. Mao, Z.P. Guo, X.B. Yu, H.K. Liu, Int. J. Hydrogen Energy 38 (2013) 3650–3660.
[11] F. Yuan, X.W. Chen, Q.F. Gu, Z.W. Tang, X.B. Yu, Int. J. Hydrogen Energy 38 (2013) 5322–5329.
[12] O.V. Komova, V.I. Simagina, N.L. Kayl, G.V. Odegova, O.V. Netskina, Y.A. Chesalov, A.M. Ozerova, Int. J. Hydrogen Energy 38 (2013) 6442–6449.
[13] Z.G. Zhang, H. Wang, J.W. Liu, M. Zhu, Thermochim. Acta 560 (2013) 82–88.
[14] U. Ulmer, J.J. Hu, M. Franzreb, M. Fichtner, Int. J. Hydrogen Energy 38 (2013) 1439–1449.
[15] D.M. Liu, C. Gao, Z.X. Qian, T.Z. Si, Q.A. Zhang, Int. J. Hydrogen Energy 38 (2013) 3291–3296.
[16] X.P. Zheng, J.J. Zheng, Q.H. Ma, S.L. Liu, X. Feng, X.B. Lin, G. Xiao, J. Alloys Compd. 551 (2013) 508–511.
[17] L. Li, F.Y. Qiu, Y.J. Wang, Y.A. Xu, C.H. An, G. Liu, L.F. Jiao, H.T. Yuan, Int. J. Hydrogen Energy 38 (2013) 3695–3701.
[18] Bogdanović, Schwickardi, J. Alloys Compd. 253–254 (1997) 1–9.
[19] X.P. Zheng, G. Xiao, S.L. Liu, X. Feng, J.J. Zheng, Int. J. Hydrogen Energy 37 (2012) 8402–8407.
[20] R.J. Xiong, G. Sang, X.Y. Yan, G.H. Zhang, X.Q. Ye, C.L. Jiang, L.Z. Luo, Int. J. Hydrogen Energy 37 (2012) 10222–10228.
[21] T. Sun, B. Zhou, H. Wang, M. Zhu, Int. J. Hydrogen Energy 33 (2008) 2260–2267.
[22] M. Fichtner, J. Engel, O. Fuhr, O. Kircher, O. Rubner, Mater. Sci. Eng. B 108 (2004) 42–47.
[23] S.Y. Zheng, F. Fang, G.Y. Zhou, G.R. Chen, L.Z. Ouyang, M. Zhu, D.L. Sun, Chem. Mater. 20 (2008) 3954–3958.
[24] J.B. Gao, P. Adelhelm, M.H.W. Verkuijlen, C. Rongeat, M. Herrich, P.J.M. van Bentum, O. Gutfleisch, A.P.M. Kentgens, K.P. de Jong, P.E. de Jongh, J. Phys. Chem. C 114 (2010) 4675–4682.
[25] T. Schmidt, L. Röntzsch, J. Alloys Compd. 496 (2010) L38–L40.
[26] Y.P. Wang, Q.L. Ren, Y.J. Wang, L. Li, D.W. Song, L.F. Jiao, H.T. Yuan, Int. J. Hydrogen Energy 35 (2010) 11004–11008.
[27] T. Wang, J. Wang, A.D. Ebner, J.A. Ritter, J. Alloys Compd. 450 (2008) 293–300.
[28] X.P. Zheng, S.L. Liu, D.L. Li, Int. J. Hydrogen Energy 34 (2009) 2701–2704.
[29] T. Wang, J. Wang, A.D. Ebner, J.A. Ritter, J. Alloys Compd. 539 (2012) 242–248.
[30] F.E. Pinkerton, J. Alloys Compd. 509 (2011) 8958–8964.
[31] S.S.-Y. Lin, J. Yang, H.H. Kung, Int. J. Hydrogen Energy 37 (2012) 2737–2741.
[32] G. Streukens, F. Schüth, J. Alloys Compd. 474 (2009) 57–60.
[33] X.L. Fan, X.Z. Xiao, L.X. Chen, S.Q. Li, Q.D. Wang, J. Alloys Compd. 509S (2011) S750–S753.
[34] J. Wang, A.D. Ebner, J.A. Ritter, Int. J. Hydrogen Energy 37 (2012) 11650–11655.
[35] Mehraj-ud-din Naik, Sami-ullah Rather, R. Zacharia, C.S. So, S.W. Hwang, A.R. Kim, K.S. Nahm, J. Alloys Compd. 471 (2009) L16–L22.
[36] J.F. Mao, Z.P. Guo, H.K. Liu, Int. J. Hydrogen Energy 36 (2011) 14503–14511.
[37] M.P. Pitt, P.E. Vullum, M.H. Sørby, M.P. Sulic, H. Emerich, M. Paskevicius, C.E. Buckley, J.C. Walmsley, R. Holmestad, B.C. Hauback, J. Alloys Compd. 514 (2012) 163–169.
[38] Y. Suttisawat, V. Jannatisin, P. Rangsunvigit, B. Kitiyanan, N. Muangsin, S. Kulprathipanja, J. Power Sources 163 (2007) 997–1002.
[39] G.J. Lee, J.H. Shim, Y.W. Cho, K.S. Lee, Int. J. Hydrogen Energy 33 (2008) 3748–3753.
[40] D. Pukazhselvan, M. Sterlin Leo Hudson, A.S.K. Sinha, O.N. Srivastava, Energy 35 (2010) 5037–5042.
[41] L. Li, Y. Wang, F.Y. Qiu, Y.J. Wang, Y.A. Xu, C.H. An, L.F. Jiao, H.T. Yuan, J. Alloys Compd. 566 (2013) 137–141.
[42] L. Li, Y.J. Wang, Y.P. Wang, G. Liu, Y. Han, F.Y. Qiu, C. Yan, D.W. Song, L.F. Jiao, H.T. Yuan, J. Alloys Compd. 509S (2011) S747–S749.
[43] X.L. Fan, X.Z. Xiao, L.X. Chen, L.Y. Han, S.Q. Li, H.W. Ge, Q.D. Wang, Int. J. Hydrogen Energy 36 (2011) 10861–10869.
[44] M.P. Pitt, P.E. Vullum, M.H. Sørby, H. Emerich, M. Paskevicius, C.E. Buckley, E. MacA. Gray, J.C. Walmsley, R. Holmestad, B.C. Hauback, J. Alloys Compd. 521 (2012) 112–120.
[45] F.Q. Zhai, P. Li, A.Z. Sun, S. Wu, Q. Wan, W.N. Zhang, Y.L. Li, L.Q. Cui, X.H. Qu, J. Phys. Chem. C 116 (2012) 11939–11945.
[46] P. Li, Q. Wan, Z.L. Li, F.Q. Zhai, Y.L. Li, L.Q. Cui, X.H. Qu, A.A. Volinsky, J. Power Sources 239 (2013) 201–206.
[47] J.W. Kim, J.H. Shim, S.C. Kim, A. Remhof, A. Borgschulte, O. Friedrichs, R. Gremaud, F. Pendolino, A. Züttel, Y.W. Cho, K.H. Oh, J. Power Sources 192 (2009) 582–587.
[48] Rafi-ud-din, L. Zhang, P. Li, X.H. Qu, J. Alloys Compd. 15 (2010) 119–128.
[49] Rafi-ud-din, X.H. Qu, P. Li, L. Zhang, M. Ahmad, J. Phys. Chem. C 115 (2011) 13088–13099.
[50] S.Y. Zheng, Y.T. Li, F. Fang, C.Y. Zhou, X.B. Yu, G.R. Chen, D.L. Sun, L.Z. Ouyang, M. Zhu, J. Mater. Res. 25 (2010) 2047–2053.
[51] X.Z. Xiao, L.X. Chen, X.H. Wang, S.Q. Li, C.P. Chen, Q.D. Wang, Int. J. Hydrogen Energy 33 (2008) 64–73.
[52] P. Wang, X.D. Kang, H.M. Cheng, J. Appl. Phys. 98 (2005) 074905.
[53] M. Sterlin Leo Hudson, H. Raghubanshi, D. Pukazhselvan, O.N. Srivastava, Int. J. Hydrogen Energy 37 (2012) 2750–2755.
[54] P. Adelhelm, J.B. Gao, M.H.W. Verkuijlen, C. Rongeat, M. Herrich, P.J.M. van Bentum, O. Gutfleisch, A.P.M. Kentgens, K.P. de Jong, P.E. de Jongh, Chem. Mater. 22 (2010) 2233–2238.
[55] G.J. Lee, J.H. Shim, Y.W. Cho, K.S. Lee, Int. J. Hydrogen Energy 32 (2007) 1911–1915.
[56] J.C. Bureau, Z. Amri, P. Claudy, J.M. Létoffé, Mater. Res. Bull. 24 (1989) 23–31.
[57] S. Gomes, G. Renaudin, H. Hagemann, K. Yvon, M.P. Sulic, C.M. Jensen, J. Alloys Compd. 390 (2005) 305–313.